Biotransformation modulates the penetration of metallic nanomaterials across an artificial blood–brain barrier model

Zhiling Guo[a,1], Peng Zhang[a,1], Swaroop Chakraborty[b], Andrew J Chetwynd[a], Fazel Abdolahpur Monikh[c], Christopher Stark[a], Hanene Ali-Boucetta[d], Sandra Wilson[e], Iseult Lynch[a], and Eugenia Valsami-Jones[a,1]

[a]School of Geography, Earth and Environmental Sciences, University of Birmingham, Birmingham B15 2TT, United Kingdom; [b]Department of Material Engineering, Indian Institute of Technology, Gandhinagar 382355, India; [c]Department of Environmental and Biological Sciences, University of Eastern Finland, FI-80101 Joensuu, Finland; [d]Nanomedicine, Drug Delivery and Nanotoxicology Laboratory, The School of Pharmacy, College of Medical and Dental Sciences, University of Birmingham, Birmingham B15 2TT, United Kingdom; and [e]Sophion Bioscience A/S, Baltorpvej 154, DK-2750 Ballerup, Denmark

Edited by Catherine J. Murphy, University of Illinois at Urbana–Champaign, Urbana, IL, and approved May 28, 2021 (received for review March 19, 2021)

Understanding the potential of nanomaterials (NMs) to cross the blood–brain barrier (BBB), as a function of their physicochemical properties and subsequent behavior, fate, and adverse effect beyond that point, is vital for evaluating the neurological effects arising from their unintentional entry into the brain, which is yet to be fully explored. This is not only due to the complex nature of the brain but also the existing analytical limitations for characterization and quantification of NMs in the complex brain environment. By using a fit-for-purpose analytical workflow and an in vitro BBB model, we show that the physiochemical properties of metallic NMs influence their biotransformation in biological matrices, which in turn modulates the transport form, efficiency, amounts, and pathways of NMs through the BBB and, consequently, their neurotoxicity. The data presented here will support in silico modeling and prediction of the neurotoxicity of NMs and facilitate the tailored design of safe NMs.

nanomaterials | blood–brain barrier | neurotoxicity | single-particle ICP-MS | synchrotron

More than a few decades have passed since the application of nanomaterials (NMs) in medicine and since the concept of nanotoxicity was formulated (1). Despite the time lapsed, concerns regarding their potential neurotoxicity (2) have yet to be fully addressed, primarily because of challenges in characterization resulting from their unique physicochemical properties. Recent studies found NMs (e.g., ZnO and magnetite NMs) can accumulate in the brain with distinct morphologies and forms that differ from their pristine counterpart, which can affect the cholinergic neurotransmission and thus brain health (3, 4). Beyond their safety, also important is the potential of NMs to act as carriers for medical interventions to the brain (e.g., to treat neurodegenerative conditions) (5).

To date, our understanding of NM biotransformation in a biological matrix and their subsequent behavior and adverse effects remains limited because of the limitation in analytical techniques capable of tracing the transformation of such small particles in biological samples. This is even more challenging when quantifying the cellular uptake of the transformed NMs, because the unique physicochemical properties of NMs (i.e., small size, high specific surface area, high free surface energy, etc.) not only can modulate their biotransformation (6) and consequently their cellular uptake but also can directly influence the cellular penetration pathway and intracellular trafficking of NMs (7). This is of paramount importance for blood–brain barrier (BBB) cells, as the penetration and trafficking pathways could influence the number and forms of NMs entering the brain and possibly exerting adverse effects to the brain (e.g., inducing neurotoxicity) (8, 9). For instance, the biotransformation of nanoparticles (e.g., ZnO) in the brain and subbrain region (hippocampus) has been reported (3, 10).

Inhaled, ingested, and dermally applied NMs can reach the blood stream (11). From there, there is a possibility that NMs in the bloodstream can cross the BBB and then directly or indirectly impact on the central nervous system (CNS) (12). The BBB is a physical barrier composed of a tightly packed layer of endothelial cells surrounding the brain, which separates the blood from the cerebrospinal fluid, allowing the transfer of oxygen and essential nutrients but preventing the access of most molecules. NMs function at the nanoscale; bind critical transport proteins such as apolipoproteins, including the brain transporter apolipoprotein E (13); and thus may have better ability to be transported across the BBB via endocytosis or diffusion (14, 15). Moreover, their biotransformation may dynamically alter their mobility and transport pathways. While emerging human (4) and in vivo (3) evidence suggests that NMs can deposit in brain regions, it is not clear whether these NMs enter the brain through the BBB pathway, what form(s) (i.e., pristine or transformed forms) and quantity of NMs enter the brain, and how the physicochemical properties of NMs modulate this penetration. Moreover, the fate of NMs within and beyond the BBB (i.e., the translocation, deposition, distribution, transformation, and adverse effect during and after crossing the BBB) is largely unknown, primarily because of the limited capacity of animal testing and difficulties in direct quantitative analysis of NMs within and beyond the

Significance

Although the brain is protected by a tight physiological guardian named the blood–brain barrier (BBB), deposition of engineered nanomaterials (ENMs) in the brain and consequent neurotoxicity has been reported. To date, it is still unclear whether and how ENMs enter the brain by crossing the BBB. In this study, we found that metallic ENMs transform in the BBB as affected by their shape, size, and intrinsic solubility, which in turn modulates their transport form, efficiency, and pathways through the BBB and, consequently, their neurotoxicity. The library of quantitative data on the chemical transformations presented here will support in silico modeling and prediction of the neurotoxicity of NMs and facilitate the tailored design of safe NMs.

Author contributions: Z.G., P.Z., S.W., I.L., and E.V.-J. designed research; Z.G., P.Z., S.C., A.J.C., and C.S. performed research; H.A.-B. contributed new reagents/analytic tools; Z.G. and P.Z. analyzed data; and Z.G., P.Z., F.A.M., and I.L. wrote the paper.

The authors declare no competing interest.

This article is a PNAS Direct Submission.

[1]To whom correspondence may be addressed. Email: z.guo@bham.ac.uk, e.valsamijones@bham.ac.uk, or p.zhang.1@bham.ac.uk.

This article contains supporting information online at https://www.pnas.org/lookup/suppl/doi:10.1073/pnas.2105245118/-/DCSupplemental.

Published July 6, 2021.

barrier at molecular and cellular levels in real time. These knowledge gaps highlight the importance of using such approaches to enable a breakthrough in our fundamental understanding of the BBB penetration ability of NMs and the relevance of physicochemical properties on controlling the path, behavior, and impacts of NMs beyond the BBB.

Here, we synthesized a library of metallic NMs with different particle compositions, sizes, and shapes and evaluated their ability to penetrate the BBB using a well-established in vitro BBB model, followed by an assessment of their behavior and fate in and beyond the BBB. To achieve this, a set of state-of-the-art analytical techniques, including single-particle inductively coupled plasma mass spectrometry (spICP-MS), synchrotron radiation–based X-ray absorption fine structure spectroscopy (XAFS), and high spatial resolution (20 nm) scanning transmission X-ray microscopy (STXM), and a series of biological assays were applied. We found that physiochemical properties of metallic NMs influenced their biotransformation in the physiological matrix. Biotransformation, in turn, modulated the transport form, efficiency, amounts, and pathways of NMs through the BBB and, consequently, the neurotoxicity. For example, spherical Ag (Ag NS) and disk-like Ag (Ag ND) NMs underwent different dissolution regimes in the physiological media and gradual transformation to Ag-sulfur compounds within the BBB, which facilitated paracellular and transcytosis entry pathways. Our finding showed that by changing the chemical composition of NMs to ZnO, CeO_2, and Fe_3O_4, the transport efficiency and amount of particles passing through the BBB change significantly, even if the shape and the size of the particles are kept the same. This can be linked to the composition-related biotransformation of the NMs, as CeO_2 and Fe_3O_4 NMs with low dissolution have the limited ability to transport across the BBB.

Results and Discussion

NM Transport Analysis across the BBB. Determining the behavior and fate of NMs, as a function of their physicochemical properties at the BBB, is not only vital for evaluating their neurological effects but also for facilitating their application, especially in targeting hard-to-reach sites within the brain when treating brain disease. Despite the valuable contribution of animal models to NM transport studies, they have limited utility in large-scale screening studies, and it remains difficult to conduct mechanistic studies and quantitative analysis at molecular and cellular levels. In vitro BBB models, which are cell-based models that can reconstitute the key structure and function of the human BBB (16), are considered a reliable and predictive screening platform for brain-penetrating agents (17). Among all available cell types, human-sourced cells show the advantages in enhancing the physiological relevance of in vitro models to the unique properties of the human BBB, providing more clinically representative data regarding NM transport, uptake, transcytosis, and toxicity (18, 19). A primary human coculture in vitro BBB model has been successfully used to investigate the transport of NMs (e.g., gold and polystyrene) across the BBB (8, 20). This was also the chosen model for our NM transport studies.

The critical barrier function of the BBB endothelium is characterized by low permeability and high expression of BBB-specific proteins such as junction proteins. Here, coculture of human primary brain microvascular endothelial cells (HBMECs) with human primary astrocytes (HAs) to generate an in vitro BBB model (Fig. 1*A*) led to stronger induction of expression of inter-endothelial tight junction proteins, including vascular endothelial (VE)-cadherin, claudin-5, and zonula occludens-1 (ZO-1) (Fig. 1*B*), than HBMECs alone. Furthermore, confocal fluorescence microscopy images demonstrated junctional protein (occludin and ZO-1) distribution at the HBMEC cell–cell borders, which form a tight barrier (Fig. 1*C*), demonstrating the reproduction of BBB-specific endothelial characteristics. Coculture with HAs in the BBB model significantly increased the transendothelial electrical resistance (TEER) values of the HBMEC monolayer from 216 to 472 $\Omega\ cm^2$ (Fig. 1*D*). The model showed size-dependent transport of fluorescently labeled dextran across the BBB, with significantly lower permeability coefficient (Pe) values than for the endothelial monoculture model (Fig. 1*E*). The TEER value and Pe to 70 kD fluorescein isothiocyanate (FITC)–dextran and 20 kD tetramethylrhodamine (TRITC)-dextran were comparable to previous BBB studies (12, 21–23), implying that the in vitro model precisely replicates key BBB features and functions and can be used for subsequent NM transport studies.

To comprehensively understand the influence of NM physicochemical properties on their ability to pass through the BBB and their subsequent fate, metallic NMs with different compositions, sizes, shapes, and dissolution profiles in physiological medium were synthesized and tested (*SI Appendix*, Table S1 and Fig. S1). This includes three sizes of CeO_2 (3 nm CeO_2, 7 nm CeO_2, and 25 nm CeO_2), two sizes of Fe_3O_4 (18 nm Fe_3O_4 and 35 nm Fe_3O_4), four shapes of Ag (Ag NS, Ag ND, rod-shaped Ag [Ag NR], and Ag nanowires [Ag NW]), and ZnO (30 nm). NMs were applied at the apical side of the model at final concentrations of 1 and 2.5 mg/L. After 48 h, medium samples from the basolateral side were taken for measurement, including quantification (elements and particles) and size determination of NMs (*SI Appendix*, Fig. S2).

In most clinical and environmental studies, mass concentrations of metallic NMs are measured to determine their uptake and transport. Although informative, this fails to provide sufficient particle-specific transport information based on which concrete conclusion can be made (e.g., particle size, particle number, particle species, etc.), which are critical for understanding and eventually predicting the behavior, fate, and long-term effect of NMs in the brain. Particle agglomeration and transformation may also occur following cellular uptake and transport into and through the BBB. Such information cannot be obtained from mass measurement alone (24), highlighting that the mass only paradigm has limitations in providing insights into the behavior of NMs in the BBB. Time-resolved spICP-MS analysis can quantify a single particle of metallic NMs at trace amounts in environmental and biological media, while simultaneously providing information on particle number concentration, size distribution, and ion concentration (25). However, the size detection limits of spICP-MS for particles varied depending on the composition elements. Therefore, not all NMs can be measured using spICP-MS. The size detection limit of spICP-MS has been shown to be 10 to 20 nm for Ag, 20 to 80 nm for ZnO and Fe_3O_4, and 10 nm for CeO_2 NMs (26). Moreover, spICP-MS calculates particle size based on the assumption that particles are spherical (26). Therefore, spICP-MS was only used for samples of 25 nm CeO_2, 18 nm Fe_3O_4, 35 nm Fe_3O_4, Ag NS, and ZnO. For other NMs, we used a different sampling strategy, as illustrated in *SI Appendix*, Fig. S2. In sampling Strategy I, spICP-MS can give both the particle concentration (particle/milliliter) and mass of ions (M_i). The mass of the transported particles (M_p) can be calculated as total element mass (M_t) subtracting the M_i. For NMs that cannot be measured by spICP-MS, sampling Strategy II was used. Assuming there were particles transported, the M_p can be calculated as M_t subtracting the M_i. The fraction of ions and particles and the total transport percentage then can be calculated.

Among all the tested NMs, ZnO exhibited the highest transport percentage, with 10.5 and 13.4% at 1 and 2.5 mg/L exposure concentrations, respectively, followed by Ag (Ag ND and Ag NS), although with a strong shape dependence (Fig. 2*A*). Our findings showed that Ag NDNMs had a higher transport (4.8% at 1 mg/L and 5.7% at 2.5 mg/L) than Ag NS NMs (2.3% at 1 mg/L and 3.1% at 2.5 mg/L). No transport was observed for Ag NR and Ag NW. This could be due to the needle-like shape of the particles, which hinders the prolongation of the cell membrane (e.g., endocytosis of the particles), as reported for silica nanowires (27). Transport of CeO_2 NMs was between 0.08 to ~0.34%, with the highest transport being observed for 3 nm CeO_2. No transport was detected for Fe_3O_4 (Fig. 2*A*). These findings clearly show

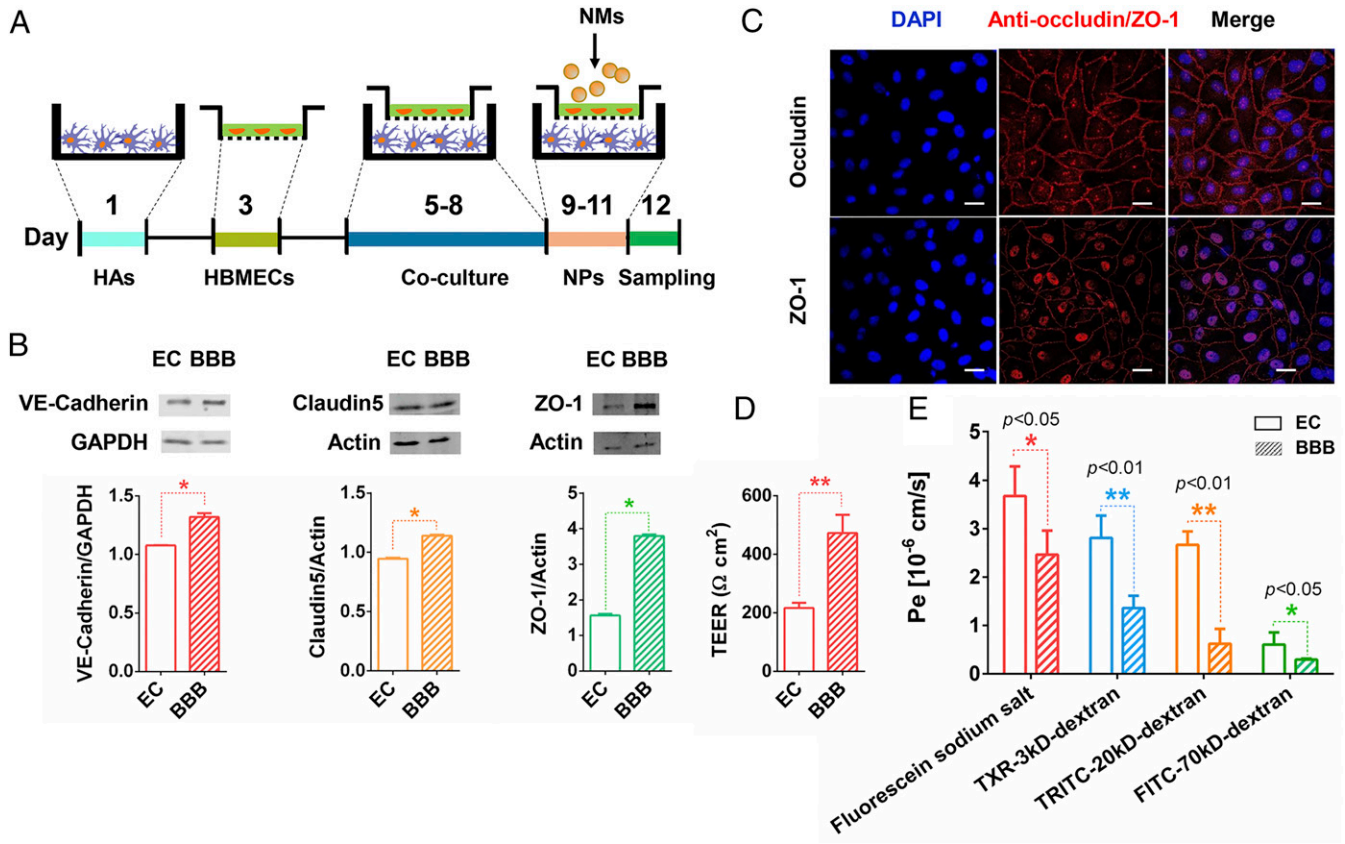

Fig. 1. In vitro BBB model. (*A*) In vitro BBB model using a coculture of HBMECs and HAs. In the apical chamber, HBMECs were cultured on a transwell insert. At the basolateral side, HAs were cultured in a 12-well plate. After the model setup, nanomaterials (NMs) were added apically, and the NM accumulation in, and transport across, the BBB was assessed after 48 h (see *Materials and Methods* for detailed information). (*B*) Western blot and densitometry analysis of VE-cadherin, claudin-5, and ZO-1 protein expression in endothelial monoculture (EC) and the in vitro BBB system (BBB). Blots were probed with anti-GAPDH/actin antibodies as a control for equal loading of cell lysates. (*C*) Fluorescence images showing the distribution of tight junction markers, ZO-1 and occludin (red), between HBMEC cells. Nuclei were stained with DAPI (blue). (*D*) TEER measurements across the HBMEC monolayer grown on the transwell insert membrane with (BBB) and without (EC) coculture with HAs. (*E*) Pe calculated from the diffusion of 70 kD FITC-dextran, 20 kD TRITC-dextran, 3 kD TXR-dextran, and fluorescein sodium salt through the HBMEC monoculture (EC) or HBMECs and HAs coculture model (BBB). Data are presented as mean ± SD ($n = 6$). All images are representative ones from at least three biological and three technical replicates. *$P < 0.05$ and **$P < 0.01$.

that variation in shape, size, and the chemical compositions of NMs can dramatically influence their penetration through the BBB. This is of paramount importance for the tailored medical application of NMs (e.g., targeted delivery system and bioimaging) and for assessing the possible risks associated with each type of metallic NMs. For all NMs, increasing the exposure concentration to 2.5 mg/L did not cause significant increase in the percentage of transported elements, suggesting that the turnover rate of the endocytotic receptors is a rate-limiting step, as shown previously for a range of other human cells (28). It is also likely that the increase in the concentration of NMs facilitates the agglomeration of NMs, which in turn reduces the transport of the agglomerates across the BBB (15). Another potential explanation is that particle agglomeration may lead to low dissolution and thus the low transport of the released ions.

The particle number concentration in the basolateral chamber, obtained by spICP-MS, differed with particle composition (Fig. 2*B*). The particle number concentration for ZnO, Ag NS, and 25 nm CeO_2 were 3.7 to 4.6 × 10^4 particles/mL, 0.95 to 1.1 × 10^4 particles/mL, and 0.4 to 0.9 × 10^3 particles/mL, respectively. We could not detect 18 nm Fe_3O_4 or 35 nm Fe_3O_4 in the basolateral chamber, although it was recently reported that magnetite NMs, which are prolific in urban, airborne particulate matter, could be found in the human brain (4). This suggests that the magnetite NMs may enter the brain through other routes, such as the olfactory pathway, rather than via the BBB. The size distribution of the transported particles was also obtained by spICP-MS, as shown in Fig. 2 *C–E* (1 mg/L) and *SI Appendix*, Fig. S3 (2.5 mg/L). The mode of the size distribution for the transported particles shifted toward a larger size compared to those of the pristine particles. This could have two explanations; first, the particles undergo agglomeration, and the agglomerates with a certain size can pass through the BBB, as each of the receptor-mediated pathways has an optimized cargo size (29, 30). Second, the particles undergo agglomeration during (i.e., in the vesicles) or after passing through the BBB.

As shown in *SI Appendix*, Fig. S2, the total mass of each element, along with its ionic and particulate form in the basolateral chamber, were acquired, and the ratio of particle to ion is shown in Fig. 2*F*. Most of the transported CeO_2 (68 to 99%) was in the form of particles, with the highest ionic fraction found for 3 nm CeO_2. In contrast, ions accounted for a much higher proportion (>75%) than particles for ZnO NMs. For Ag NM, the ratio of transported particles to ions was shape dependent. For Ag NS, more than 64% of the transported Ag was in the form of particles, while for Ag ND most of the transported Ag was ionic (>76%). These results showed that higher ionic fraction was correlated with higher total transport percentage, which was confirmed by linear regression analysis (Fig. 2*G*) ($R^2 = 0.7570$). This implies that the dissolution of partially soluble NMs can contribute to

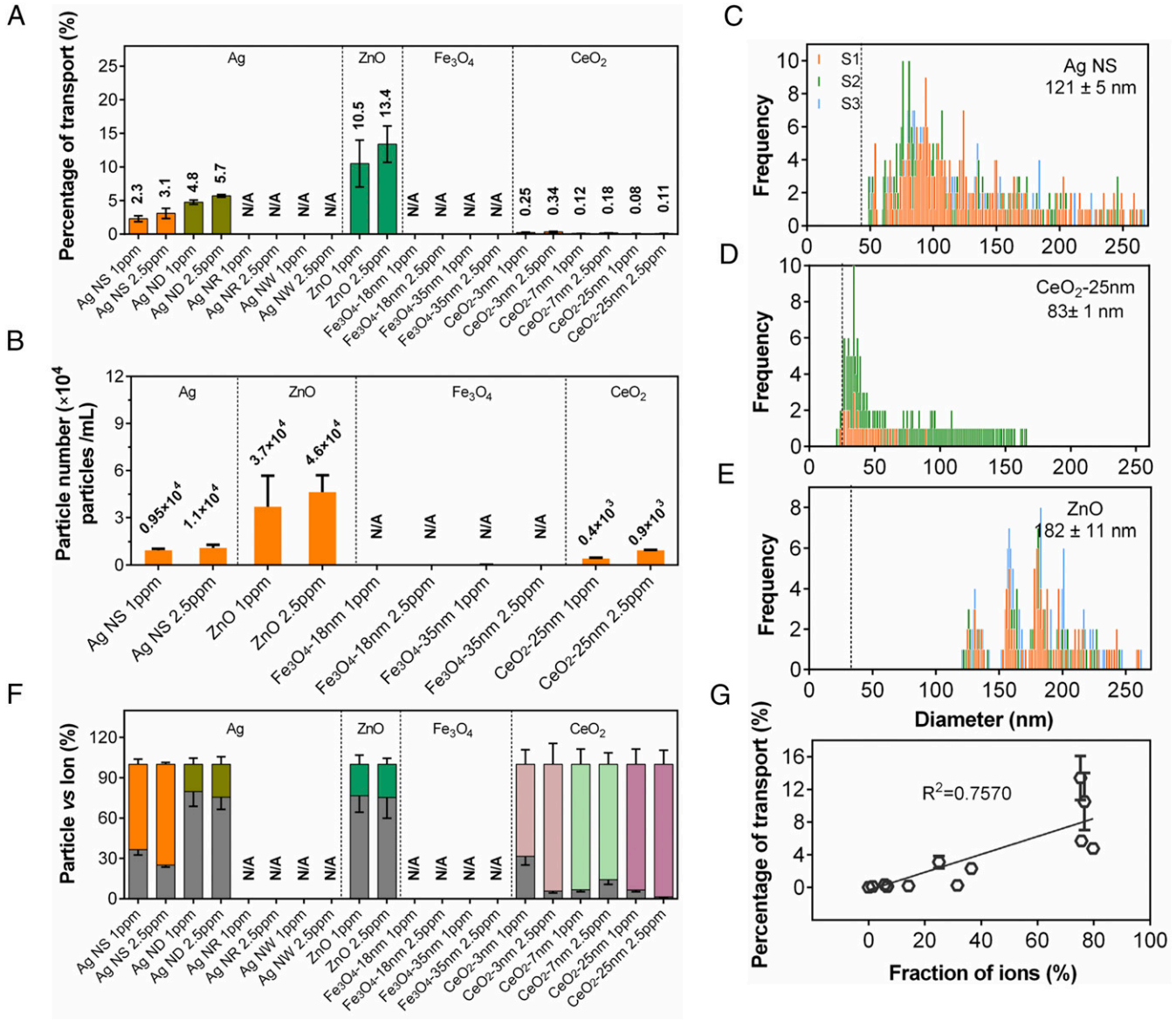

Fig. 2. NM transport across the BBB. (*A*) Percentage of total transported elements in the basolateral chamber for different NMs at 1 and 2.5 mg/L (parts per million). (*B*) Particle number concentration (particle/milliliter) in the basolateral medium. (*C–E*) Size distribution of transported particles at 1 mg/L (parts per million): Ag NS (*C*), 25 nm CeO_2 (*D*), and ZnO (*E*). S1, S2, and S3 indicate three sample replicates. The vertical dashed lines indicate the average sizes of the pristine NMs. (*F*) Ratio of particle versus ion in the total transported elements. The upper columns are the ratios of particles, and the lower columns are the ratio of ions. (*G*) Linear regression analysis showing that the percentage of transported elements correlated positively with the mass fraction of ions, $n = 3$. The *x*-axis indicates the transported ions (percentage) for different NMs, and the *y*-axis indicates the corresponding total transported elements (percentage) for each NM. N/A indicates that no element or particle were detected either by the ICP-MS or spICP-MS method.

the transport of NMs across BBB. To confirm this, we measured the dissolution of NMs in the culture medium.

NM Passage across the BBB Is Associated with Particle Dissolution. The dissolution of all NMs in water was much lower than in endothelial cell growth medium 2 (EGM-2) medium (Fig. 3 *A–D*). Among all the NMs, ZnO showed the highest dissolution (~45%) in cell medium after 48 h incubation, followed by Ag (3 to 26.5%) (Fig. 3 *A* and *B*). Different shapes of Ag showed different dissolution in the following order: Ag ND > Ag NS > Ag NR and Ag NW (Fig. 3*A*). The exposed crystal facets highly affect the reactivity (e.g., dissolution) of NMs. Ag ND was characterized with highly reactive (111) facet as the basal plane and high levels of surface defects, thus presenting high reactivity (31), which contributed to the higher dissolution of Ag ND than other shaped Ag NMs. In comparison, Ag NS with a similar size showed lower dissolution in the medium, suggesting that shape had a profound effect on the dissolution of Ag NMs, as reported previously (32). Ag NR and Ag NW with high aspect ratios and relatively larger sizes showed a low dissolution. Compared to ZnO and Ag, the dissolution of Fe_3O_4 and CeO_2 NMs was quite low in the cell culture medium (1.5 to 2.0% for Fe_3O_4 and 0.2 to 0.9% for CeO_2) (Fig. 3 *C* and *D*). This is in accordance with previous reports that CeO_2 NMs are relatively stable in environmental and biological surroundings (33). In addition, size effects on dissolution were observed for Fe_3O_4 and CeO_2 NMs, with smaller-sized NMs showing a little higher ion release (Fig. 3 *C* and *D*). This could be due to the relatively higher particle numbers and, consequently, a higher total surface area of smaller-sized NMs available for ion release. Further linear regression analysis showed that the NM passage through the BBB

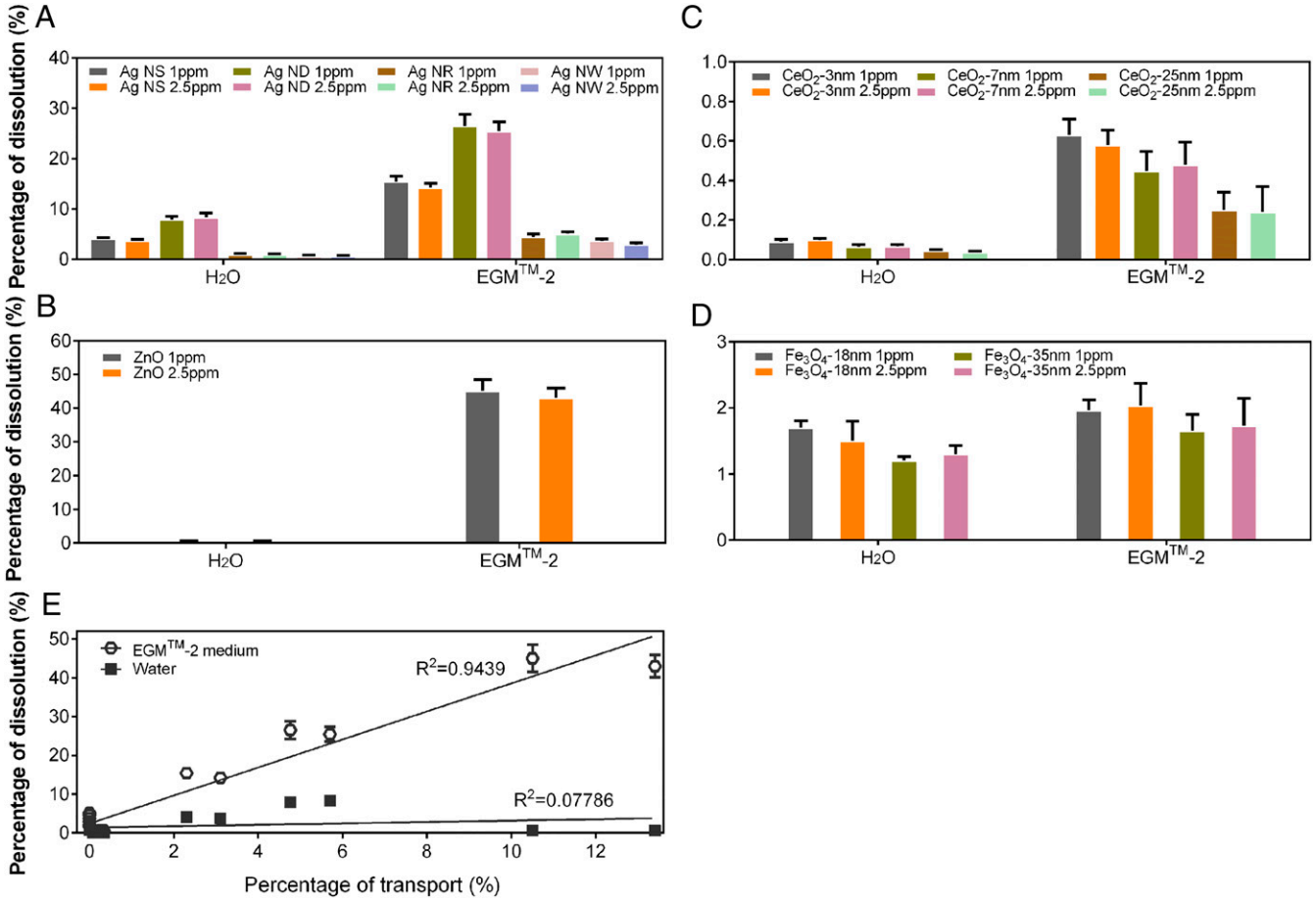

Fig. 3. NM passage through the BBB is associated with NM dissolution in the medium. (*A–D*) Dissolution (percentage) of NMs in deionized water and EGM-2 medium after 48 h of incubation. Ag (*A*), ZnO (*B*), CeO_2 (*C*), and Fe_3O_4 (*D*) NMs. (*E*) Linear regression analysis showing that the percentage of transported elements correlated positively with the NM dissolution in the EGM-2 medium ($R^2 = 0.9439$) but not in water ($R^2 = 0.07786$), $n = 6$. The *x*-axis indicates the total transported elements (percentage) for different NMs, and the *y*-axis indicates the corresponding dissolution (percentage) in water or EGM-2 medium for each NM.

was positively associated with the NM dissolution in the cell medium (Fig. 3*E*; $R^2 = 0.9439$) but not in water ($R^2 = 0.07786$).

NMs Enhance BBB Permeability. Transport of compounds from blood to brain occurs via two possible routes (i.e., passive diffusion and active transport). For NMs, the main transport route is considered to be the transcytosis process, which commences NM uptake by endocytosis, followed by intracellular vesicular trafficking and exocytosis to the basolateral side (19). Although the passive transport of compounds is limited because of the physiological nature of the BBB and its tight junctions, in cases in which the BBB permeability was enhanced, through damage for example, NMs can also cross the BBB between the cells in a process called paracellular transport and access the brain (34, 35). We examined the impact of NMs on BBB permeability after 48 h exposure by testing the flux of 70 kD FITC-dextran, 20 kD TRITC-dextran, 3 kD Texas Red (TXR)-dextran, and fluorescein sodium salt across the barrier after it had been exposed to NMs. Results showed that the Pe to 70 kD FITC-dextran, 20 kD TRITC-dextran, and 3 kD TXR-dextran were all increased after exposure to 2.5 mg/L Ag NS, Ag ND, and ZnO. Pe of fluorescein sodium salt did not show a significant change, except for ZnO (Fig. 4). Other NMs at either concentration did not affect the BBB permeability. Next, we examined the toxicity of NMs to the HBMECs. As shown in *SI Appendix*, Fig. S4, all the NMs showed no effects on the cell viability after 24 and 48 h exposure at 1 mg/L, while the viability was decreased by 12.6 and 23.7%, respectively, in the Ag NS and Ag ND group at 2.5 mg/L, after 48 h of exposure. The cell viability was decreased by 15.8% after 48 h of exposure to ZnO NMs. Cell viability in the 3-nm CeO_2 treatment was increased, which is consistent with previous report that CeO_2 has a role in neuroprotection because of its antioxidative enzyme-mimicking activity, which can capture the reactive oxygen species, thus protecting the cells (36). Fe_3O_4 NMs of different sizes and CeO_2 of the other two sizes (−7 nm and 25 nm) showed no effects on the cell viability at 48 h. The malondialdehyde (MDA) content in HBMECs was increased when exposed to 2.5 mg/L Ag NS, Ag ND, and ZnO NMs for 48 h (*SI Appendix*, Fig. S5), indicating some cellular damage. Together, these data indicate that the higher concentration (2.5 mg/L) of Ag NS, Ag ND, and ZnO NMs may impair the cell growth and cause cell membrane damage, which can lead to the enhanced BBB permeability and thus lead to NM access to the brain observed. The BBB plays a vital role in the maintenance of brain homeostasis and the physiological environment of the CNS by strictly restricting the passage of various chemical substances and foreign molecules from the brain vasculature into the brain. The impaired BBB integrity will compromise the health of the CNS and increase the permeability of foreign substances including NMs (e.g., Ag and ZnO) from the peripheral blood into the brain, which may eventually cause damage to the brain (neurotoxicity).

HA cell viability in the BBB was also decreased in the Ag ND and Ag NS treatments at 2.5 mg/L after 48 h (*SI Appendix*, Fig. S6), indicating that Ag ND and Ag NS exert neurotoxicity, as also

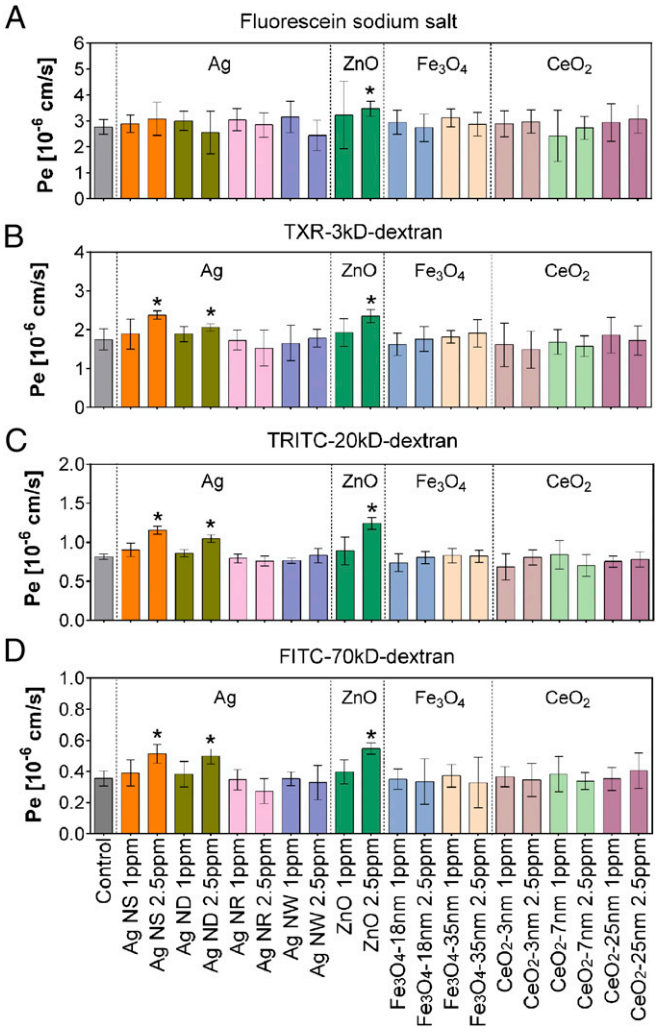

Fig. 4. NM effect on BBB permeability after 48 h exposure. (*A–D*) Flux of fluorescently labeled dextran across the BBB determined after 48 h exposure to 1 and 2.5 mg/L NMs. Fluorescein sodium salt (*A*), 3 kD TXR-dextran (*B*), 20 kD TRITC-dextran (*C*), and 70 kD FITC-dextran (*D*). Data are presented as mean ± SD ($n = 6$). *$P < 0.05$ indicates significant difference compared to the unexposed control.

reported previously for other Ag NMs (9) after passing through the BBB. In the Ag ND and Ag NS groups, a high percentage of ionic silver (Ag^+) was detected on the basolateral side (Fig. 2*C*), so the observed neurotoxicity to HA may arise from the Ag^+ released from Ag ND. Together, these results suggest that Ag NS, Ag ND, and ZnO may transport paracellularly across the BBB, as a result of the enhanced BBB permeability at the higher exposure concentration, and after crossing the endothelial cell layer, they can cause toxicity to brain cells.

NMs Cross the BBB through Transcytosis-Mediated Routes. Here, we focused on Ag and CeO_2 NMs as representatives since they showed distinct dissolution and transport ability. The Ag and Ce elements in the HMBEC cells were quantified by ICP-MS after 24 and 48 h of NM exposure. As shown in Fig. 5 *A–D*, cellular uptake of CeO_2 and Ag NMs clearly showed a time and dose dependence. For Ag NMs, the highest uptake was observed for Ag ND, with 235 and 825 ng Ag being detected at the 1- and 2.5-mg/L treatments, respectively, after 48 h exposure. This accounts for 47 and 66% of the total applied Ag, respectively. The uptake of Ag NR and Ag NW only accounted for 3.4 to 9.7% of the total applied Ag. CeO_2 uptake was between 1.5 to 2.3% (7.6 to 28.6 ng) and was size dependent, with the −3-nm size showing a little higher uptake than −7 and −25 nm CeO_2. The low uptake of CeO_2 was consistent with the finding that a very small amount of CeO_2 was transported to the basolateral side (Fig. 2*A*).

The exocytosis process was studied by replacing the NM-containing medium on both sides of the BBB (transwell) 24 h after exposure with fresh NM-free medium and monitoring the elemental concentration in the basolateral side for 48 h. After the medium containing Ag/CeO_2 NMs was discarded, HBMECs can exocytose Ag or Ce from the cells into the new replaced medium. The Ag or Ce elements at the apical (exoapical) and basolateral (exobasolateral) medium were then quantified by IC-PMS. After the medium change for 24 and 48 h, Ag or Ce elements were detected on the basolateral side (except Ag NR and Ag NW), suggesting NM passage through the BBB via exocytosis. No Ag NR and Ag NW were detected, which may be because of their specific shape, large size, and low uptake. However, the NMs that transported through transcytosis-mediated routes were relatively low. The total detected elements in the basolateral medium only accounted for <5% (Ag NMs) and <10% (CeO_2 NMs) of the cell uptake amount at all time points, suggesting accumulation of NMs in the BBB itself. The elemental mass in the basolateral medium constitutes only 5 to 10% (Ag NMs) and 0.7 to 9% (CeO_2) of the total exocytosed amount after 48 h. Therefore, only a very small portion of exocytosed NMs were directed to the basolateral side. For Ag NR and Ag NW, Ag was only detected in apical medium, suggesting that they did not cross the BBB but instead transported into the BBB and back out to the bloodstream side (apical chamber), possibly by a transport protein such as P-glycoprotein (37).

The mass of total transported elements can be roughly considered as the sum of the elements exocytosed to the basolateral side and that transported paracellularly. The masses of Ag NS and ND exocytosed to basal side at 48 h were 8.9 ± 2.2 ng and 21.4 ± 5.9 ng, respectively, at the 1-mg/L exposure concentration, which showed no significant difference from the total transported mass at 1 mg/L (12 ± 4 ng and 28 ± 4 ng). However, at 2.5 mg/L, the exocytosed Ag masses (14 ± 2.4 ng and 34 ± 5 ng for Ag NS and Ag ND, respectively) were lower than the total transported mass (39 ± 1.3 ng and 65 ± 6.7 ng). This result indicated that at low concentration, transcytosis was the main transport pathway for Ag NMs, while at high concentration, there was another pathway, such as paracellular transport (Fig. 4), in addition to transcytosis, as observed in the section of *NMs Enhance BBB Permeability*. For CeO_2 NMs, the total transported mass showed no difference with that exocytosed to the basolateral side at both exposure concentrations, suggesting that transcytosis was the main transport route.

NMs Transformation in the BBB. NMs are highly dynamic and prone to transformation in biological systems (38), which affects the transport of NMs into and across the BBB. To further understand the process of the transport, transformation of Ag and CeO_2 NMs in the BBB and following transcytosis to the basal chamber was analyzed. Synchrotron radiation-based bulk XAFS, which is a powerful method to determine and quantify the chemical species of elements in a biological matrix (39), can provide insights into the transformation of NMs in the BBB and after crossing the BBB. It was employed to analyze the chemical species of the Ag and CeO_2 NMs after uptake by HBMECs. Fig. 6*A* shows the Ag K-edge X-ray absorption near edge structure (XANES) spectra and the fractions of different Ag species, obtained by linear combination fitting (LCF) analysis of the XANES spectra, using different Ag compounds as standard references (*SI Appendix*, Fig. S7). The LCF analysis provided good fits to the original experimental spectra (fitting lines are shown as bubbles in Fig. 6*A*; the full fitting parameters are shown in *SI Appendix*, Table S2). Results showed that the Ag in Ag NS–, Ag NR–, and Ag NW–treated HBMECs exhibited similar features as that of the original Ag NMs, while the

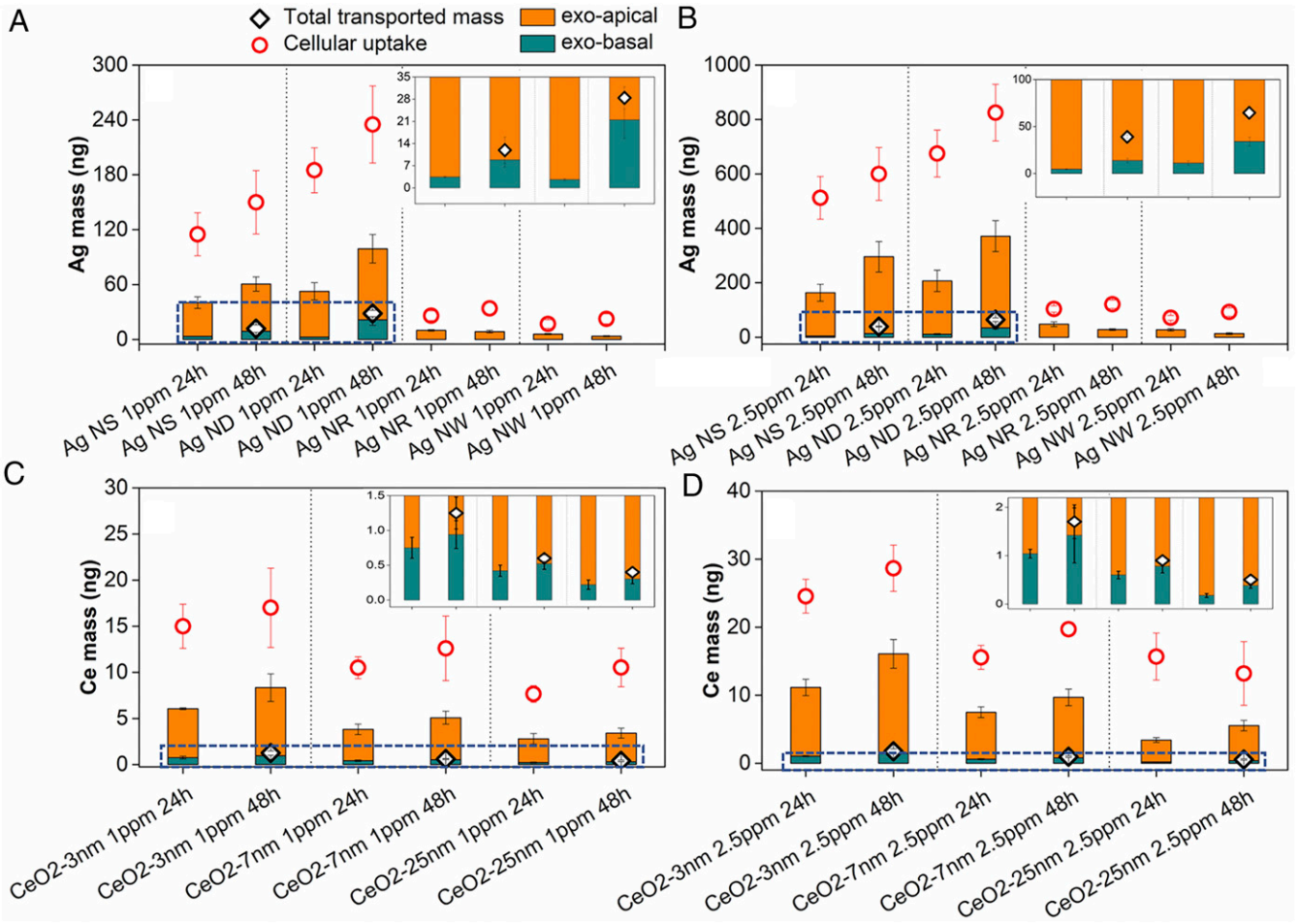

Fig. 5. Cellular uptake and exocytosis of Ag and Ce in HBMECs 24 and 48 h after replacing the NM-containing medium with fresh NM-free medium. (*A*) Exposure to 1 mg/L Ag NMs. (*B*) Exposure to 2.5 mg/L Ag NMs. (*C*) Exposure to 1 mg/L CeO_2 NMs. (*D*) Exposure to 2.5 mg/L CeO_2 NMs. Open circles indicate elemental mass in HBMECs; the diamonds indicate the total mass transported to the basolateral chamber; and orange and green bars indicate the elements that were exocytosed to the apical and basolateral sides, respectively. The inner image is a magnification of the dashed rectangle area in each panel.

Ag in Ag ND–treated HBMECs exhibited features similar to Ag-cysteine, a representative Ag-sulfur–binding species (Fig. 6*A*). LCF analysis revealed that the dominant Ag species was still the particle form in Ag NS– (82.1%), Ag NR– (93.6%), and Ag NW– (95.1%) treated HBMECs, with a small proportion being transformed to Ag-cysteine (Fig. 6*B*). In comparison, in Ag ND–treated HBMECs, nearly 40% of the Ag had transformed into Ag-cysteine. A similar phenomenon was reported in THP-1 cells, in which Ag NMs gradually transformed to Ag-sulfur compounds during the uptake and exocytosis processes (40). In cells, there are abundant peptides, proteins, and antioxidant molecules, which are composed of sulfur-containing cysteine, cystine, and methionine moieties. Silver has a high affinity for sulfur, so upon entering the cell, Ag NMs encounter various organic substances that promote the release of Ag^+ ions, which may coordinate with these moieties by binding with sulfur. Also, the Ag^+ can induce the accumulation of reactive oxygen species, which oxidize the surface of Ag NMs and further promote the release of Ag^+ (40).

The transformation of Ag NMs was further shown by mapping the Ag chemical species in situ in Ag ND– and Ag NS–treated HBMECs using STXM. STXM provided the in situ distribution of the Ag species, as shown by the phase mapping (Fig. 6*C*). Cluster 1 was identified as Ag species by the L-edge near edge X-ray absorption fine structure (NEXAFS) spectra extracted from the phase mapping. As seen from the optical density image (gray images) and the phase mapping, Ag was observed in the cells in both Ag ND and Ag NS groups. The chemical species of the Ag clusters in Ag ND and Ag NS groups were identified as a mixture of particulate Ag and Ag-cysteine, as shown by fitting of the NEXAFS spectra using Ag reference compounds (Fig. 6*C*). There was 62 and 38% of particulate Ag and Ag-cysteine in the Ag ND group and 74 and 26% in Ag NS group, respectively. The results are in accordance with that obtained by bulk XAFS, confirming that transformation of Ag NMs in cells occurred, with more transformation being observed for Ag ND because of its higher solubility, compared to the other Ag NM shapes (Fig. 3*A*).

The Ce in 3 nm CeO_2-, 7 nm CeO_2-, and 25 nm CeO_2-treated HBMECs was mainly present as CeO_2 (Fig. 6*D*). The transformed species, Ce acetates, which originate from the binding of Ce^{3+} with carboxyl groups, only accounted for 0 to 4.3%. Although the transformation of CeO_2 NMs was minimal, the percentage of Ce acetates showed a size dependence, with the smallest sized CeO_2 showing more transformation (Fig. 6*E*).

We also determined the chemical species of Ag and CeO_2 NMs in the solids collected after 48 h of incubation in EGM-2 medium (*SI Appendix*, Figs. S8 and S9). Results showed that for Ag NMs the solids remained mainly as particulate Ag, with only 3 and 8% in the form of AgCl for Ag NS and Ag ND, respectively. For Ag NR, Ag NW, and CeO_2 NMs, the solids were 100% Ag or CeO_2 particles after incubation, suggesting that no solid products formed. Together with the dissolution data (Fig. 3), the results suggest that Ag NMs might be taken up by cell in the form of both

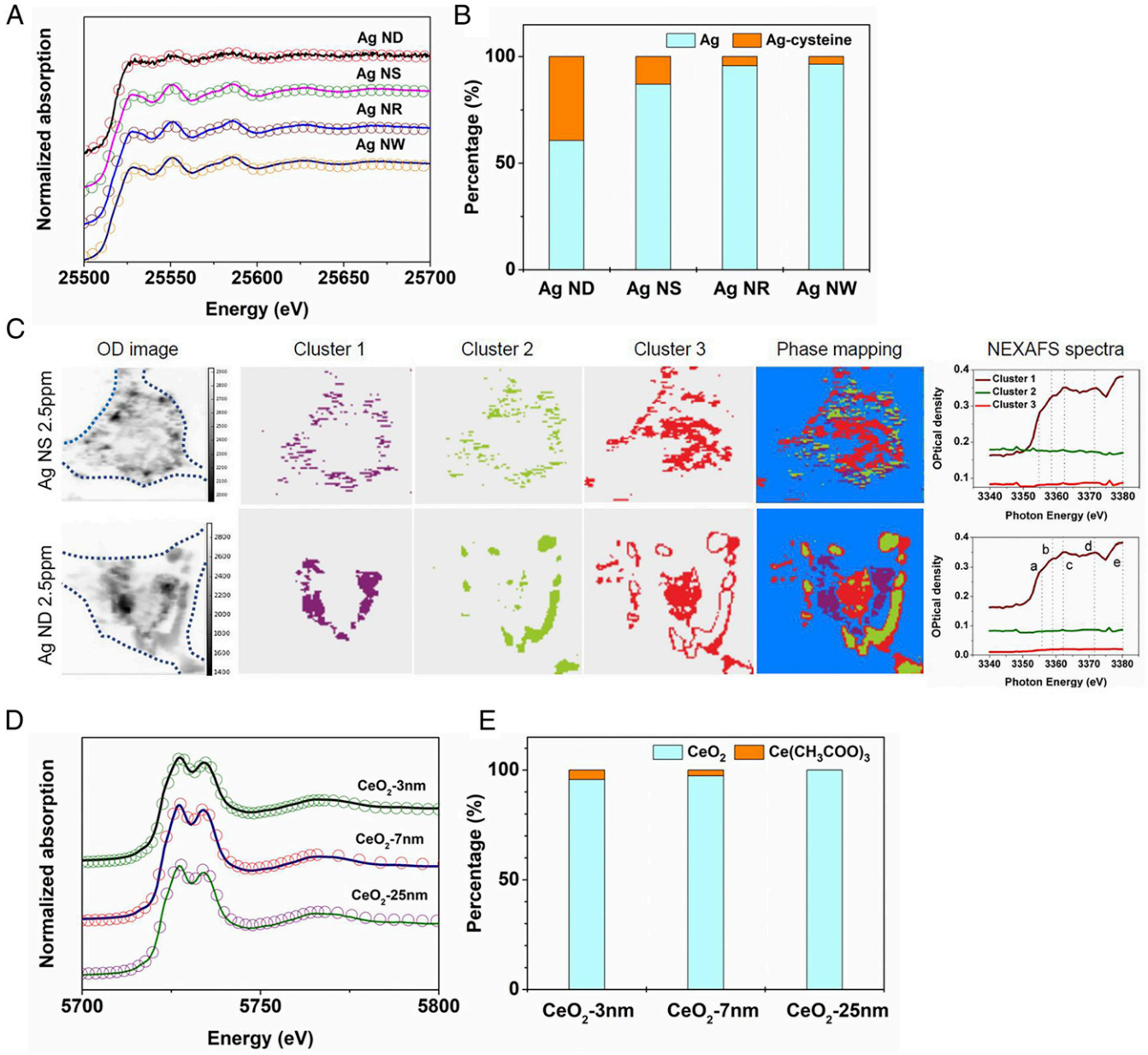

Fig. 6. NM transformation in the HBMECs of the BBB. (*A*) Ag K-edge XANES spectra of the HBMECs in the BBB model. The solid lines indicate the original spectra. The bubble lines indicate the fitting obtained from LCF analysis. (*B*) The fractions of the Ag species obtained by LCF analysis. (*C*) STXM images of Ag ND and Ag NS in HBMECs. The gray images (optical density images) were the transmission images of the cells. Clusters 1 to 3 indicate the distribution (clustering) of the three different compositions obtained by cluster analysis. The STXM image (the phase mapping) was the overlay of the cluster images. Ag L-edge NEXAFS spectra were subtracted from the STXM image. (*D*) Ce K-edge XANES spectra in the HBMECs in the BBB model. (*E*) The fractions of the Ce species obtained by LCF analysis.

particles and ions, while CeO_2 NMs are mainly taken up as particles. Although AgCl was detected in the solids of Ag NS and Ag ND, it was not detected in the cells (Fig. 6), which agrees with previous study by Wang et al. that Ag-cysteine and particulate Ag are the main species in cells (40).

We also collected cocultured HA samples from the Ag ND and Ag NS exposed groups to examine whether we can detect Ag XAFS spectra. Interestingly, we were able to get the Ag spectra in HAs from both groups (*SI Appendix*, Fig. S10). LCF analysis revealed that 22 and 46% of Ag presented as Ag-cysteine in the Ag NS and Ag ND groups, respectively, with the rest being particles (Fig. 6*G*). The fractions of Ag-cysteine in HAs were higher compared with that observed in HBMECs, indicating that more transformation occurred during the Ag NM transport. These results also confirm that Ag was also internalized by HAs at the basolateral side after crossing through the BBB, which poses a risk to neuronal cells of the brain. It should be noted that in vivo the BBB contains endothelial cells of the capillary wall, astrocyte end-feet ensheathing the capillary, and pericytes embedded in the capillary basement membrane. Based on our results that biotransformation occurred in both endothelial cells and astrocytes, it is also possible that NMs can be taken up by pericytes and undergo biotransformation after crossing the BBB.

In summary, we examined the behavior, fate, and adverse effects of several metal-based NMs in an in vitro BBB model and found that Ag and ZnO NMs, which are widely and largely used

in various daily consumer products and healthcare products, have the potential to cross the BBB and enter the brain in the form of both particles and dissolved ions, depending on the physiochemical properties of NMs, either through the paracellular space by modulating the BBB permeability or through transcytosis-mediated routes. Moreover, they can also adversely affect the health of astrocyte cells after entering the brain in the pristine or transformed form. While significant uptake of NMs into the BBB was observed, very little was transcytosed to the basolateral (brain) side, with significant amounts being recycled back to the apical (bloodstream) side (Fig. 7). Paracellular transport was only observed at the higher concentration tested (2.5 mg/L) and was associated with membrane damage and NM dissolution. XANES and STXM provided important insights into the form of the Ag and Ce internalized by the BBB and transcytosed to the basolateral (brain) side. The data presented in our study provide important insights into NMs interactions with, and transport through and from, the BBB and will facilitate the tailored design of NMs with the desired bioeffects and the development of in silico models to predict NMs uptake, transformation, and transport across the BBB.

Materials and Methods

Cell Culture. HBMECs (H-6023, 2BScientific) and HAs (CC-2565, Lonza) were incubated at 37 °C in a water-saturated, 5% CO_2 incubator. Both primary cells were used between passages 3 and 5 for all experiments.

NMs. NMs are homemade or purchased. Details of the synthesis and characterization are described in *SI Appendix*. For the transport experiment, the concentrated NM stock solution was centrifuged to remove any ions that had been released during storage. The solutions were then immediately aliquoted. One aliquot was taken to measure the nanoparticle concentration using ICP-MS; the others were frozen by liquid nitrogen and stored at −80 °C. The frozen aliquots were taken upon use, and the exposure media were prepared by diluting the stock in EGM-2 medium, based on the ICP-MS determined concentration. With this centrifuge step, all the ions in the stock are removed before cellular exposure.

BBB Model Setup. The BBB model was composed of a coculture system, containing an insert with HBMECs grown on the polyester membrane at the luminal side and a 12-well plate at the bottom with Has at the abluminal side (Fig. 1*A*). In addition to the coculture system, inserts without cells or medium, inserts with EGM-2 medium only, or inserts with HBMECs alone were setup as comparisons and controls. The BBB model was verified by testing the expression of VE-cadherin, claudin-5, and ZO-1, using immunocytochemistry and the Western blot method, and the permeability using fluorescently labeled chemicals. TEER was measured using an Endohm-12G chamber and an Epithelial Volt/Ohm Meter (World Precision Instruments). Detailed information is described in *SI Appendix*.

NM Transport Study. Detailed information of all NMs tested are shown in *SI Appendix*, Table S1. At day 9, differentiation medium in the luminal side of the inserts was replaced with EGM-2 medium containing NMs with final concentrations of 1 and 2.5 mg/L. The medium in the 12-well plates was replaced with fresh EGM-2 medium. Following 24 and 48 h of Ag and CeO_2 NM exposure, HBMEC cells were collected for element analysis by ICP-MS. Medium from the 12-well plates was sampled after 48 h for spICP-MS or ICP-MS measurements (*SI Appendix*, Tables S3 and S4) to analyze the transported particles and ions, respectively, as well as the total elemental mass (*SI Appendix*, Fig. S2). HBMECs and HAs were collected for XAFS or STXM analysis. The integrity of the barrier after NM exposure was measured.

NM Toxicity to HBMECs and HAs. The toxicity of NMs to the HBMECs and HAs after adding NMs to the apical side was tested after 24 and 48 h NM application to the BBB model using the cell counting kit-8 assay (Abcam) according to the manufacturer's instructions. MDA content was measured as a lipid peroxidation marker using a lipid peroxidation (MDA) assay kit (Abcam) according to the manufacturer's instructions.

Dissolution of NMs. Dissolution of all NMs in deionized water and EGM-2 medium was assessed by measuring the ions released into the solution. Briefly, NM suspensions were prepared and mixed in deionized water or EGM-2 medium at 1 and 2.5 mg/L at 37 °C for 48 h. Samples were centrifuged at 11,000 × *g* for 15 min. The supernatants were collected and diluted with 2% nitric acids for ICP-MS analysis, as described in section of *NM Transport Study*. The pellets were collected to analyze the Ag and Ce species in the solids by XAFS.

Ag and CeO_2 NM Uptake and Exocytosis in HBMECs. The BBB model was setup, as mentioned in section of *BBB Model Setup*. At day 9, NMs' (Ag NS, Ag NR, Ag NW, Ag ND, 3 nm CeO_2, 7 nm CeO_2, and 25 nm CeO_2) suspensions were added to the luminal side of the inserts with the final concentrations of 1 and 2.5 mg/L.

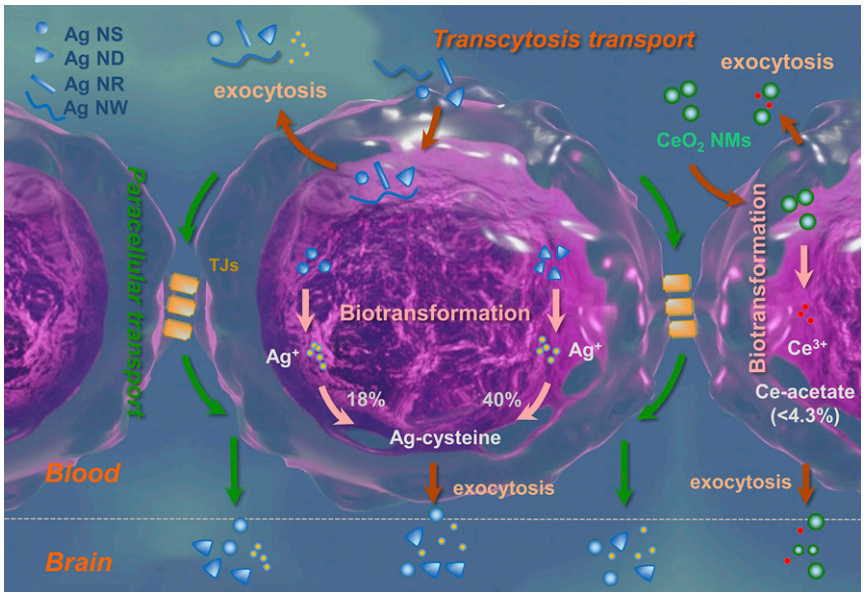

Fig. 7. A schematic diagram of the uptake, biotransformation, transport, and fate of representative NMs, Ag and CeO_2 NM, in and across the BBB. A significant uptake of Ag ND and Ag NS into the BBB was observed; however, very little was transcytosed to the basolateral (brain) side of the BBB model, with significant amounts being recycled back to the apical (bloodstream) side and limited retention in the BBB cells. Paracellular transport was only observed at the higher concentration tested and was associated with membrane damage and NM dissolution. Very limited uptake into or transport across the BBB of CeO_2 NMs was observed, which correlates with their low solubility.

After 24 h of exposure, NM suspension from the luminal side of inserts and the medium in the basolateral chamber were removed, followed by a rinsing of the cells five times with 1× phosphate-buffered saline. Then, cells were further cultured for 24 and 48 h in fresh (NM free) EGM-2 medium. The medium in the apical and basolateral sides were then collected for ICP-MS analysis.

Ag and CeO_2 NM Transformation. The transformation of NMs following uptake into, and transport through, the BBB was examined by synchrotron-based XAFS techniques and in situ soft STXM, as described in *SI Appendix*.

Statistical Analysis. Data are expressed as mean ± SD and were analyzed with GraphPad InStat software (GraphPad Software, Inc.) and OriginPro 9.1. Student's *t* test was applied for comparison between control and different treatments. One-way ANOVA was used for the comparison of different groups. Differences are considered as statistically significant at values of $P < 0.05$ and $P < 0.01$.

Data Availability. All study data are included in the article and/or *SI Appendix*.

ACKNOWLEDGMENTS. This work was supported by the Horizon 2020 (H2020) Marie Skłodowska-Curie Individual Fellowships research program (NanoBBB, Grant Agreement 798505, Z.G. Fellow; NanoLabels, Grant Agreement 750455, P.Z. Fellow). Additional support from the H2020 European Union research infrastructure for nanosafety project NanoCommons (Grant Agreement 731032), for data management and the Horizon 2020 project ACEnano (Grant H2020-NMBP-2016-720952), and for analytical support are acknowledged. This work was carried out with the support of Diamond Light Source instrument STXM (beamline I08, proposal SP20567-2) and instrument core X-ray absorption spectroscopy (beamline B18, proposal SP20204-2). We thank Giannantonio Cibin and Diego Gianolio at the B18 beamline for their support during XANES experiments and Tohru Araki and Burkhard Kaulich at I08 beamline for their support during STXM experiments. Rachel Smith from Public Health England is acknowledged for early discussion of project design.

1. E. Valsami-Jones, I. Lynch, NANOSAFETY. How safe are nanomaterials? *Science* **350**, 388–389 (2015).
2. Z. Guo *et al*., Elucidating the mechanism of the surface functionalization dependent neurotoxicity of graphene family nanomaterials. *Nanoscale* **12**, 18600–18605 (2020).
3. Z. Guo *et al*., Intranasal exposure to ZnO nanoparticles induces alterations in cholinergic neurotransmission in rat brain. *Nano Today* **35**, 100977 (2020).
4. B. A. Maher *et al*., Magnetite pollution nanoparticles in the human brain. *Proc. Natl. Acad. Sci. U.S.A.* **113**, 10797–10801 (2016).
5. R. Meenambal, M. M. Srinivas Bharath, Nanocarriers for effective nutraceutical delivery to the brain. *Neurochem. Int.* **140**, 104851 (2020).
6. H. Wang *et al*., Toxicity, bioaccumulation, and biotransformation of silver nanoparticles in marine organisms. *Environ. Sci. Technol.* **48**, 13711–13717 (2014).
7. P. Foroozandeh, A. A. Aziz, Insight into cellular uptake and intracellular trafficking of nanoparticles. *Nanoscale Res. Lett.* **13**, 339 (2018).
8. M. N. Raghnaill *et al*., Paracrine signalling of inflammatory cytokines from an in vitro blood brain barrier model upon exposure to polymeric nanoparticles. *Analyst* **139**, 923–930 (2014).
9. N. Repar *et al*., Silver nanoparticles induce neurotoxicity in a human embryonic stem cell-derived neuron and astrocyte network. *Nanotoxicology* **12**, 104–116 (2018).
10. Z. Guo, P. Zhang, H. Q. Xie, B. Zhao, I. Lynch, First in vivo evidence for compromised brain energy metabolism upon intranasal exposure to ZnO nanoparticles. *Environ. Sci. Technol. Lett.* **7**, 315–322 (2020).
11. V. De Matteis, Exposure to inorganic nanoparticles: Routes of entry, immune response, biodistribution and in vitro/in vivo toxicity evaluation. *Toxics* **5**, 29 (2017).
12. S. I. Ahn *et al*., Microengineered human blood-brain barrier platform for understanding nanoparticle transport mechanisms. *Nat. Commun.* **11**, 175 (2020).
13. J. Kreuter *et al*., Apolipoprotein-mediated transport of nanoparticle-bound drugs across the blood-brain barrier. *J. Drug Target.* **10**, 317–325 (2002).
14. S. Bhaskar *et al*., Multifunctional nanocarriers for diagnostics, drug delivery and targeted treatment across blood-brain barrier: Perspectives on tracking and neuroimaging. *Part. Fibre Toxicol.* **7**, 3 (2010).
15. M. N. Ragnaill *et al*., Internal benchmarking of a human blood-brain barrier cell model for screening of nanoparticle uptake and transcytosis. *Eur. J. Pharm. Biopharm.* **77**, 360–367 (2011).
16. C.-F. Cho *et al*., Blood-brain-barrier spheroids as an in vitro screening platform for brain-penetrating agents. *Nat. Commun.* **8**, 15623 (2017).
17. S. Bagchi *et al*., In-vitro blood-brain barrier models for drug screening and permeation studies: An overview. *Drug Des. Devel. Ther.* **13**, 3591–3605 (2019).
18. M. Campisi *et al*., 3D self-organized microvascular model of the human blood-brain barrier with endothelial cells, pericytes and astrocytes. *Biomaterials* **180**, 117–129 (2018).
19. D. J. Mc Carthy, M. Malhotra, A. M. O'Mahony, J. F. Cryan, C. M. O'Driscoll, Nanoparticles and the blood-brain barrier: Advancing from in-vitro models towards therapeutic significance. *Pharm. Res.* **32**, 1161–1185 (2015).
20. S. A. Jensen *et al*., Spherical nucleic acid nanoparticle conjugates as an RNAi-based therapy for glioblastoma. *Sci. Transl. Med.* **5**, 209ra152 (2013).
21. P. M. D. Watson *et al*., Modelling the endothelial blood-CNS barriers: A method for the production of robust in vitro models of the rat blood-brain barrier and blood-spinal cord barrier. *BMC Neurosci.* **14**, 59 (2013).
22. V. Siddharthan, Y. V. Kim, S. Liu, K. S. Kim, Human astrocytes/astrocyte-conditioned medium and shear stress enhance the barrier properties of human brain microvascular endothelial cells. *Brain Res.* **1147**, 39–50 (2007).
23. E. S. Lippmann *et al*., Derivation of blood-brain barrier endothelial cells from human pluripotent stem cells. *Nat. Biotechnol.* **30**, 783–791 (2012).
24. F. Abdolahpur Monikh *et al*., A dose metrics perspective on the association of gold nanomaterials with algal cells. *Environ. Sci. Technol. Lett.* **6**, 732–738 (2019).
25. F. Abdolahpur Monikh *et al*., Method for extraction and quantification of metal-based nanoparticles in biological media: Number-based biodistribution and bioconcentration. *Environ. Sci. Technol.* **53**, 946–953 (2019).
26. S. Lee *et al*., Nanoparticle size detection limits by single particle ICP-MS for 40 elements. *Environ. Sci. Technol.* **48**, 10291–10300 (2014).
27. J. F. Zimmerman *et al*., Cellular uptake and dynamics of unlabeled freestanding silicon nanowires. *Sci. Adv.* **2**, e1601039 (2016).
28. E. J. Guggenheim, J. Z. Rappoport, I. Lynch, Mechanisms for cellular uptake of nanosized clinical MRI contrast agents. *Nanotoxicology* **14**, 504–532 (2020).
29. E. J. Guggenheim *et al*., Refining in vitro models for nanomaterial exposure to cells and tissues. *NanoImpact* **10**, 121–142 (2018).
30. H. Hillaireau, P. Couvreur, Nanocarriers' entry into the cell: Relevance to drug delivery. *Cell. Mol. Life Sci.* **66**, 2873–2896 (2009).
31. S. George *et al*., Surface defects on plate-shaped silver nanoparticles contribute to its hazard potential in a fish gill cell line and zebrafish embryos. *ACS Nano* **6**, 3745–3759 (2012).
32. C. Graf *et al*., Shape-dependent dissolution and cellular uptake of silver nanoparticles. *Langmuir* **34**, 1506–1519 (2018).
33. T. Xia *et al*., Comparison of the mechanism of toxicity of zinc oxide and cerium oxide nanoparticles based on dissolution and oxidative stress properties. *ACS Nano* **2**, 2121–2134 (2008).
34. H. Meng, W. Leong, K. W. Leong, C. Chen, Y. Zhao, Walking the line: The fate of nanomaterials at biological barriers. *Biomaterials* **174**, 41–53 (2018).
35. C. Buzea, I. I. Pacheco, K. Robbie, Nanomaterials and nanoparticles: Sources and toxicity. *Biointerphases* **2**, MR17–MR71 (2007).
36. B. A. Rzigalinski, C. S. Carfagna, M. Ehrich, Cerium oxide nanoparticles in neuroprotection and considerations for efficacy and safety. *Wiley Interdiscip. Rev. Nanomed. Nanobiotechnol.* **9**, e1444 (2017).
37. G. Siegel, R. W. Albers, S. Brady, D. Price, Eds., *Basic Neurochemistry: Molecular, Cellular, and Medical Aspects*, (Elsevier, 7th Ed., 2005).
38. G. V. Lowry, K. B. Gregory, S. C. Apte, J. R. Lead, Transformations of nanomaterials in the environment. *Environ. Sci. Technol.* **13**, 6893–6899 (, 2012).
39. P. Zhang *et al*., Biotransformation of ceria nanoparticles in cucumber plants. *ACS Nano* **6**, 9943–9950 (2012).
40. L. Wang *et al*., Use of synchrotron radiation-analytical techniques to reveal chemical origin of silver-nanoparticle cytotoxicity. *ACS Nano* **9**, 6532–6547 (2015).